CHEMISTRY OF MATERIALS

Article

pubs.acs.org/cm

Identifying the Structure of the Intermediate, $Li_{2/3}CoPO_4$, Formed during Electrochemical Cycling of $LiCoPO_4$

Fiona C. Strobridge,[†,‡] Raphaële J. Clément,[†,‡] Michal Leskes,[‡] Derek S. Middlemiss,[‡,§] Olaf J. Borkiewicz,[⊥] Kamila M. Wiaderek,[⊥] Karena W. Chapman,[⊥] Peter J. Chupas,[⊥] and Clare P. Grey*[,‡,#]

[‡]Department of Chemistry, University of Cambridge, Lensfield Road, Cambridge, Cambridgeshire CB2 1EW, United Kingdom

[⊥]X-ray Science Division, Advanced Photon Source, Argonne National Laboratory, Argonne, Illinois 60439, United States

[#]Department of Chemistry, State University of New York at Stony Brook, Stony Brook, New York 11794-3400, United States

Supporting Information

ABSTRACT: In situ synchrotron diffraction measurements and subsequent Rietveld refinements are used to show that the high energy density cathode material $LiCoPO_4$ (space group *Pnma*) undergoes two distinct two-phase reactions upon charge and discharge, both occurring via an intermediate $Li_{2/3}(Co^{2+})_{2/3}(Co^{3+})_{1/3}PO_4$ phase. Two resonances are observed for $Li_{2/3}CoPO_4$ with intensity ratios of 2:1 and 1:1 in the ^{31}P and ^{7}Li NMR spectra, respectively. An ordering of Co^{2+}/Co^{3+} oxidation states is proposed within a $(a \times 3b \times c)$ supercell, and Li^+/vacancy ordering is investigated using experimental NMR data in combination with first-principles solid-state DFT calculations. In the lowest energy configuration, both the Co^{3+} ions and Li vacancies are found to order along the *b*-axis. Two other low energy Li^+/vacancy ordering schemes are found only 5 meV per formula unit higher in energy. All three configurations lie below the $LiCoPO_4$–$CoPO_4$ convex hull and they may be readily interconverted by Li^+ hops along the *b*-direction.

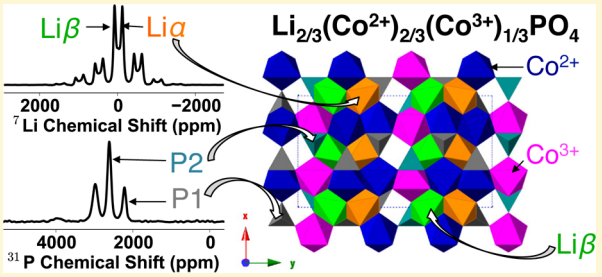

INTRODUCTION

Olivine-type $LiFePO_4$[1] has been extensively studied as a promising cathode material for Li-ion batteries, due to its good reversibility, safe operating voltage (3.45 V vs Li/Li^+) and high reversible capacity[2] of 160 mAh/g (compared to the practical capacity of 140 mAh/g for $LiCoO_2$,[3] the commonly used cathode in the portable communications industry). However, the low operating voltage of $LiFePO_4$ leads to an energy density that is considered low for use in electric transportation. Substituting Fe^{2+} with a transition metal that has a higher redox potential (e.g., Mn^{2+}, Co^{2+}, or Ni^{2+} with redox potentials of 4.1, 4.8, and 5.1 V, respectively, vs Li/Li^+)[4−6] increases the theoretical energy density of the olivine cathode material. However, $LiMnPO_4$, $LiCoPO_4$, and $LiNiPO_4$[7,8] have more sluggish kinetics than isostructural $LiFePO_4$, and are more difficult to fully lithiate and delithiate. $LiCoPO_4$ has the lowest hole polaron migration barrier of the high voltage olivines and subsequently has the highest electronic conductivity among $LiMnPO_4$, $LiCoPO_4$ and $LiNiPO_4$.[9−12] Furthermore, the high redox potential of the Co^{2+}/Co^{3+} couple means that $LiCoPO_4$ has a high theoretical energy density of 800 Wh/kg, as compared with 580 Wh/kg for $LiFePO_4$, but is not as affected as $LiNiPO_4$ by the electrolyte decomposition that occurs at high voltages.[13,14]

Bramnik et al. in 2007 studied the electrochemical reaction of $LiCoPO_4$ using in situ X-ray diffraction (XRD) and observed an intermediate $Li_{0.7}CoPO_4$ phase, where the composition was determined based on Vegard's Law (i.e., assuming a linear relationship of the unit cell parameters to Li content).[15] However, a later study combining X-ray and neutron diffraction determined an intermediate $Li_{0.6}CoPO_4$ stoichiometry.[16] Thus, the Li content of this phase likely lies in the range 0.6 and 0.7, but it is not clear whether the difference in Li content arises from the ability of the intermediate phase to tolerate some degree of solid solution, or whether it reflects differences in the approaches used to estimate the Li content. Loss of long-range order was also observed, which agrees with the chemical delithiation results of Wolfenstine et al.[17,18]

The observation of intermediates in the olivine system is not unique to $LiCoPO_4$. Intermediates of Li_xFePO_4 $(0.5 < x < 0.7)$ have been observed on cooling the solid solution phases formed at elevated temperatures,[19,20] from chemical oxidation[21] and more recently, during electrochemical cycling of micron-sized particles.[22] The isolated intermediates generally have a Li content of between 0.6 and 0.7, the Li content again being typically inferred using Vegard's Law. First-principles density functional theory (DFT) calculations performed on the $Li_{0.6}FePO_4$ phase found that it is energetically favorable for Li

Received: July 21, 2014
Revised: October 7, 2014
Published: October 9, 2014

   dx.doi.org/10.1021/cm502680w | Chem. Mater. 2014, 26, 6193−6205

vacancies to be ordered in pairs.[21] An $A_{2/3}$ intermediate (A = Na, Li) has also been observed during charging of the polyanionic materials $NaFePO_4$ and $LiVPO_4F$.[23,24] The crystal structure of the Na phase, $Na_{2/3}FePO_4$ (space group *Pnma*), was originally proposed to have a $(3a \times 3b \times c)$ supercell (relative to the parent olivine unit cell),[25,26] in which the Fe^{3+} cations are aligned in the (110) and (220) planes and the Na^+ vacancies reside between the Fe^{3+} ions for charge balance.[26,27] Boucher et al., on the basis of TEM and synchrotron data showed, however, that this cell could be redrawn using a smaller "$(a-b \times 3b \times c)$" monoclinic *P21/n* superstructure, which is only 3 times larger in volume than the original cell.[28] DFT calculations suggested that $Li_{2/3}FePO_4$ adopts the same superstructure.[28]

The $LiCoPO_4$–$CoPO_4$ system exhibits complex magnetic properties, the magnetic data providing insight into the electronic structures of the end and intermediate members, and of direct relevance to the present study, often aiding the interpretation of the nuclear magnetic resonance (NMR) spectroscopy. Ehrenberg et al. carried out an experimental magnetic study on the end member $LiCoPO_4$ and $CoPO_4$ phases, and on their intermediate Li_xCoPO_4 (x = 0.6) phase, and showed that the electronic ground state of all three compositions is high spin.[16] High-spin $LiCoPO_4$ and $CoPO_4$ ground states had also previously been predicted using DFT plus Hubbard U (DFT+U) calculations, and self-consistently calculated effective Hubbard U parameters for Co^{2+} and Co^{3+}.[29] The result for the fully delithiated Co^{3+}-only phase is not necessarily expected given that the electronic configuration of Co^{3+} is d^6, for which a low spin configuration (corresponding to a fully occupied t_{2g} orbital set in octahedral coordination) is typically lower in energy than the high spin $(t_{2g})^4(e_g)^2$ configuration. Additionally, an intermediate spin Co^{3+} has been reported to exist at the surface of $LiCoO_2$, owing to changes in the Co–O coordination near and at particle surfaces,[30] and in Li-excess $LiCoO_2$ materials.[31] A magnetic and neutron diffraction study on a $LiCoPO_4$ polycrystalline sample reported an antiferromagnetic alignment of the Co spins, along the [010] vector in the *Pnma* unit cell.[32] Ehrenberg et al.'s neutron diffraction study confirmed this alignment of spins, and found a similar alignment of the Co spins in their intermediate Li_xCoPO_4 (x = 0.6) phase.[16] The neutron diffraction data acquired on a sample with average composition of $Li_{0.2}CoPO_4$ was interpreted in terms of an additive contribution from all three stable phases ($LiCoPO_4$, $Li_{0.6}CoPO_4$, and $CoPO_4$), and the magnetic structure of $CoPO_4$ was found to comprise of Co spins aligned antiferromagnetically along the [100] direction of the $CoPO_4$ unit cell (i.e., perpendicular to the spin alignment in the $LiCoPO_4$ cell).

In situ X-ray (powder) diffraction is a valuable tool for monitoring the evolution of the long-range order of crystalline battery materials during electrochemical cycling.[33−35] Solid-state NMR, on the other hand, yields insight into the local coordination of the nucleus being studied and is also proven to be a fundamental technique for the study of battery materials.[36−38] The paramagnetic Co^{2+} and Co^{3+} ions in the olivine structure result in hyperfine interactions between the unpaired electrons and the nucleus under study (^{7}Li and ^{31}P in this case), and these interactions dominate the NMR response. The strongly covalent P–O bonds in the olivine structure lead to a large transfer of electron density onto the P atom via Co–O–P pathways, the resulting through-bond or supertransferred Fermi contact interaction leading to very large ^{31}P isotropic shifts (e.g., $\delta_{iso} \approx 3000$ ppm for $LiCoPO_4$).[39] The through-space nuclear-electron interaction (i.e., the dipolar interaction) in these systems results in broad spinning sideband manifolds, even when fast magic angle spinning (MAS) is used. The presence of multiple chemical environments invariably complicates the spectra, as the isotropic resonance due to one environment may overlap with spinning sidebands from another, and so pulse sequences that separate sidebands from isotropic resonances are particularly useful in such cases. For example, both the magic angle turning phase adjusted sideband separation (MATPASS) and the adiabatic magic angle turning (aMAT) experiments have been used to study related paramagnetic cathode materials;[40,41] the former method is used in this work.

This paper builds on our preliminary report of the ^{31}P spectra and XRD patterns of Li_xCoPO_4[42] and on the work recently published by Kaus et al.[43] We combine the complementary experimental techniques of NMR and XRD with first-principles DFT calculations to study the electrochemical (de)lithiation of $LiCoPO_4$. We obtain invaluable insights into not only how $LiCoPO_4$ delithiates, but also into the Co^{2+}/Co^{3+} ordering and the Li composition of the Li_xCoPO_4 intermediate phase. Because only limited information is obtained experimentally on Li^+/vacancy ordering in the intermediate phase, we use DFT calculations to evaluate the lowest energy configurations, within the Co^{2+}/Co^{3+} ordering determined from the experimental NMR and XRD data on the intermediate phase. The effect of the magnetic ordering and spin states of the Co^{2+} and Co^{3+} cations on the phase energetics is explored by DFT, first for the end member phases, and then for the intermediate Li_xCoPO_4 structure.

EXPERIMENTAL AND DFT DETAILS

Synthesis and Characterization. Carbon-coated $LiCoPO_4$ (C-$LiCoPO_4$) was synthesized via the solid-state method using cobalt oxalate (Sigma-Aldrich), lithium carbonate (Sigma-Aldrich, 99.997%), ammonium dihydrogen phosphate (Sigma-Aldrich, 99.999%) and 10 wt % Ketjen black (AzkoNobel) in a stoichiometric mixture. After high-energy ball milling for 20 min, the reaction mixture was pelletized and heated to 600 °C under flowing argon. The precursors were heated for 6 h, cooled and reheated for 11 h twice, before a final 24 h heating step.[44] The additional heating and cooling steps were carried out to decrease the amount of impurities present in the final product.

Phase purity was confirmed using powder X-ray diffraction with a PANalytical Empyrean X-ray diffractometer with a Cu Kα source. The total scan time was 9 h and 52 min, using a step size of 0.017° over a 2θ range from 5 to 140°. The TOPAS software was used to perform the Rietveld refinement.[45]

Film Fabrication and Battery Assembly for Electrochemical Testing and ex Situ NMR. The electrode was prepared by ball milling 80 wt % C-$LiCoPO_4$, 10 wt % carbon super P Li (Timcal) and 10 wt % polyvinylidene fluoride (Kynar) for 1 h. Dry *N*-methyl pyrolidene (Sigma-Aldrich) was added dropwise to the mixture to make a slurry. A 150 μm spreader was used to cast the film onto aluminum foil, which was dried in an oven at 60 °C overnight. A circular punch of 7/16 in. diameter was used to cut the cathode (~2 mg). For the ex situ NMR studies, the as-synthesized C-$LiCoPO_4$ powder (~10–20 mg) was used as the cathode. A coin cell-type battery was assembled in an argon-filled glovebox, using Li metal (Sigma-Aldrich) as the counter electrode, a Whatman GF/B borosilicate microfiber filter as the separator and 1 M $LiPF_6$ solution in a 1:1 mixture of ethylene carbonate/dimethyl carbonate as the electrolyte.

Film Fabrication and Battery Assembly for in Situ XRD. The electrode was prepared by mixing 85 wt % C-$LiCoPO_4$, 5 wt % Super P carbon (Alfa Aesar), 5 wt % carbon black (Vulcan XC-72, Cabot

dx.doi.org/10.1021/cm502680w | *Chem. Mater.* 2014, 26, 6193−6205

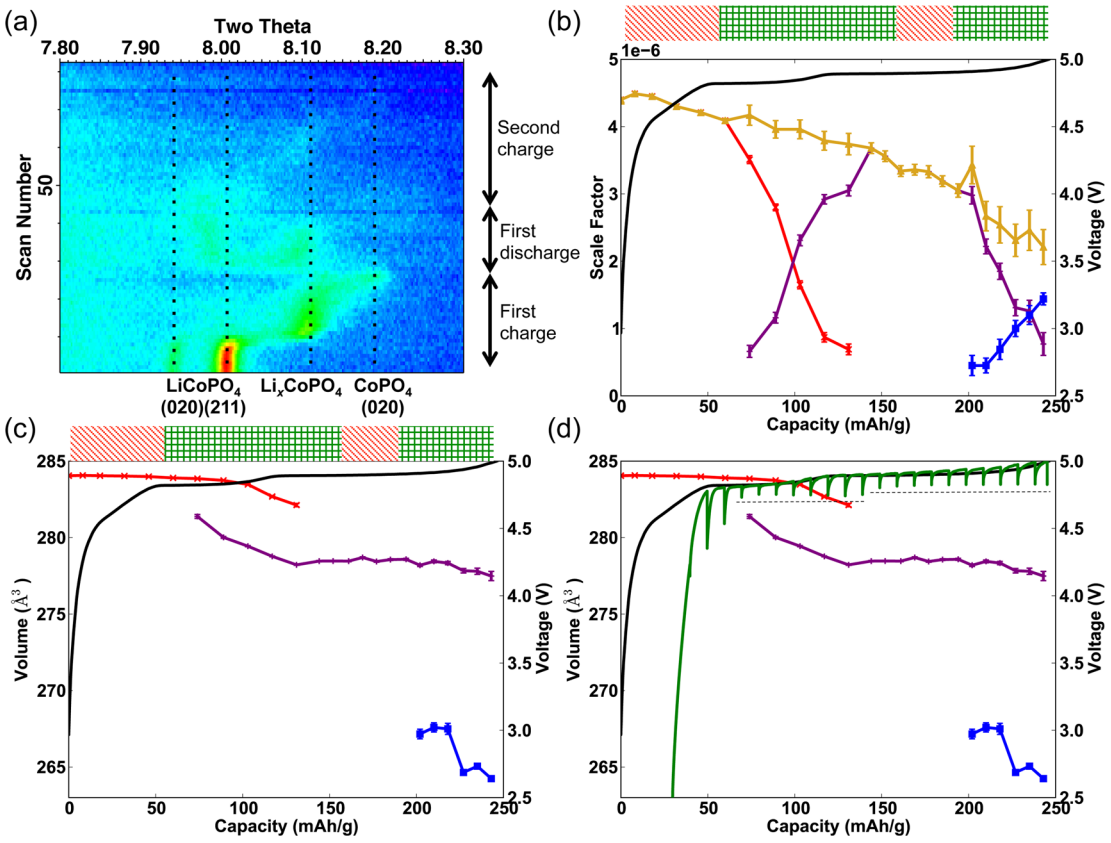

Figure 1. XRD data for the first 1.5 galvanostatic cycles of $LiCoPO_4$ cycled at a rate of $C/20$. (a) Two-dimensional image of the patterns at a 2θ range of 7.8−8.3°, shows the transformation of the (211) and (020) reflections in $LiCoPO_4$ and $CoPO_4$. The *y*-axis is scan number (time) and *x*-axis is 2θ. The results from the Rietveld refinements using the Topas Academic software[35] show changes in (b) the scale factor (the sum of the scale factors is plotted in yellow) and (c) the unit cell volume in the three phases ($LiCoPO_4$, Li_xCoPO_4 and $CoPO_4$ shown in red, purple and blue, respectively). (d) GITT experiment (in green) for $LiCoPO_4$ (4th charge) is overlaid onto the unit-cell volume data obtained for the 1st charge; the OCV is indicated with a black dotted line.

Corporation) and 5 wt % polytetrafluorethylene (Sigma-Aldrich). The powder was pressed into a 13 mm-diameter pellet of ∼150 μm thickness and weighing ∼22 mg. The pellet was assembled into the AMPIX[46] in situ cell in an argon-filled glovebox, using Li metal as the counter electrode, a Whatman GF/B borosilicate microfiber filter as the separator, and 1 M $LiPF_6$ solution in a 1:1 mixture of ethylene carbonate/dimethyl carbonate as the electrolyte (Tomiyama Pure Chemical Industries).

In Situ XRD. In situ XRD experiments were performed at the powder diffraction beamline, 11-BM, at the Advanced Photon Source at Argonne National Laboratory. High angular resolution X-ray diffraction data were collected using a 12 channel analyzer detector array (λ = 0.413609 Å, beam size 1.5 × 0.5 mm).[47] Data spanning a 0−26° 2θ range were collected using a step size of 0.002°. Each measurement took 7 min 40 s. Rietveld refinements were undertaken within the Topas Academic software.[45]

Ex Situ NMR. Hahn echo and MATPASS spectra were collected on a Bruker 200 Avance III spectrometer (4.7 T field strength) at a Larmor frequency of 81 and 78 MHz for the ^{31}P and ^{7}Li experiments, respectively, using a 1.8 mm MAS Samoson probe. For the ^{31}P MATPASS experiments a series of five 90° pulses with a pulse width of 1.6 μs were employed, rotor synchronized at a MAS frequency of 38−39 kHz.[40] The recycle delay was 0.015 s. The decay time constant of the Hahn echo/MATPASS sequence, T_2', was obtained at 4.7 T for Li_xCoPO_4 using a series of Hahn echoes where τ, the delay separating the centers of the 90° and 180° pulses, was varied between 250 μs and 16 ms in 8 increments. The signal decay was then fitted with an exponential function. The rotors were packed by mixing KBr and the partially cycled C-$LiCoPO_4$ composite electrode in a 2:1 ratio, in order to reduce paramagnetic interactions with the field that prevented the rotors from spinning. The ^{31}P and ^{7}Li data were referenced to an 85 wt % H_3PO_4 and 1 M LiCl aqueous solution, respectively, at 0 ppm.

DFT Calculations. Configurations with different spin states and spin alignments were generated for $LiCoPO_4$, $CoPO_4$, and for the intermediate phase (assumed to be $Li_{2/3}CoPO_4$ as discussed below), and their energetics were computed in a series of solid-state DFT simulations. The Vienna Ab Initio Simulation Package (VASP5.2)[48−51] was implemented within spin-polarized DFT,[52,53] and the projector-augmented wave (PAW) approach[54,55] was used to describe the electron−ion core interaction. Full relaxation of the atomic positions and cell parameters, and total energy calculations, were carried out in the absence of symmetry constraints. The Perdew−Burke−Ernzerhof (PBE) exchange-correlation functional[56,57] was used throughout, applying the Hubbard U model[58,59] within the rotationally invariant formalism proposed by Liechstenstein et al.[60] to correct for the known deficiencies of pure functionals for highly localized 3d states, as explained in more detail below.[4] After testing for convergence of the total energy of the $LiCoPO_4$ and $CoPO_4$ end members with respect to the plane wave cutoff energy and k-point mesh density, a cutoff energy of 500 eV and a 24 k-point grid were selected for calculations within the 4 formula unit cells of the end member compounds. A smaller k-point grid (16 k-points) was used for the ($a \times 3b \times c$) $Li_{2/3}CoPO_4$ supercells comprising 12 formula units. The threshold difference for self-consistent field (SCF) convergence in the total free energy was set to 1×10^{-5} eV, and a Gaussian-type smearing of the Fermi level, equivalent to a temperature of 1.2 K, was applied. Starting structures for the end member phases were taken from a previous study by Ehrenberg et al.,[16] whereas the optimization of the intermediate phase proceeded from the $LiCoPO_4$ structure in which a third of the Li^+ ions were removed.

dx.doi.org/10.1021/cm502680w | *Chem. Mater.* 2014, 26, 6193−6205

The effect of spin polarization on the total energy of the different Li_xCoPO_4 phases (x = 0, 2/3, 1) was investigated by initializing each Co spin in a particular spin configuration (low spin $t_{2g}^6e_g^1$ or high spin $t_{2g}^5e_g^2$ for d^7 Co^{2+} ions; and low spin $t_{2g}^6e_g^0$, high spin $t_{2g}^4e_g^2$, or intermediate spin $t_{2g}^5e_g^1$ for Co^{3+} ions) in the SCF process. The intermediate spin configuration was explored since it has been found in other Co^{3+} systems.[30,31] The total magnetization of the cell was fixed to the value corresponding to the initial magnetic spin configuration (equal to the sum of all individual Co spins in ferromagnetic cells, or to zero in antiferromagnetic cells) in the first structural optimization run, but the total cell magnetization constraint was released in a subsequent structural optimization run. The charge density was recalculated at the start of each new optimization and single point energy run, from the wave function obtained at the end of the previous run. The final energy, and spin and charge distributions of the different configurations were obtained from a single point energy run in the absence of magnetic constraints.

Values of 5.05 and 6.34 eV were chosen for the effective Hubbard interaction parameter $U_{eff} = U - J$ for Co^{2+} (in $LiCoPO_4$) and Co^{3+} (in $CoPO_4$), respectively, where U is the intraband Coulomb term and J is the intraatomic exchange term. The U_{eff} values were obtained self-consistently and used successfully in a previous study on the $LiMPO_4$ compounds (M = Mn, Co, Ni, Fe).[29] To compare the total energies obtained for the various Li configurations with stoichiometry $Li_{2/3}CoPO_4$ to the total energies obtained for the $LiCoPO_4$, and $CoPO_4$ end members, a single U_{eff} value of 5.48 eV was assumed for all phases. This value is the weighted average of the U_{eff} values optimized for Co^{2+} in $LiCoPO_4$ and Co^{3+} in $CoPO_4$, assuming Co^{2+} and Co^{3+} are present in a 2:1 ratio. The effect of using a single U_{eff} value to calculate the energies of the end member $LiCoPO_4$ and $CoPO_4$ compounds is further discussed in the Supporting Information (SI). Moreover, the effect of electronic localization, through the use of a U Hubbard correction term, on the energies of the different spin and magnetic states of the end member $LiCoPO_4$ and $CoPO_4$ phases, and on the formation energies of the different intermediate configurations, was further explored by repeating all calculations in the ferromagnetic state within the pure GGA approach (U = 0 eV). Table S2 in the Supporting Information summarizes the outcome of all the calculations carried out in this study.

RESULTS AND DISCUSSION

Synthesis and Characterization of $LiCoPO_4$. Carbon coated $LiCoPO_4$ (C-$LiCoPO_4$), *Pnma*, was synthesized via the solid-state method.[44] Additional heating steps beyond that used in the $LiFePO_4$ synthesis[44] were required to decrease the amount of impurities present in the product (including Li_3PO_4 and Co_2P; see the Supporting Information). XRD and solid-state ^{31}P and ^7Li NMR experiments were carried out on C-$LiCoPO_4$ and there were no detectable impurities (see the Supporting Information). The unit-cell parameters evaluated from a Rietveld refinement on the XRD pattern agree well with literature values (a = 10.202(48) Å, b = 5.922(28) Å, c = 4.700(23) Å and volume =283.9(24) Å^3).[16] A single isotropic resonance is observed in both the ^{31}P and ^7Li NMR spectra (δ_{iso} of 2985 ppm and −104 ppm, respectively) as expected from single distinct P and Li environments in $LiCoPO_4$.

Diffraction and Electrochemical Studies. In situ XRD was carried out on the C-$LiCoPO_4$-composite film in the AMPIX cell[46] for 1.5 galvanostatic cycles at a charge rate of C/20 (see the Supporting Information). A two-dimensional representation of the XRD patterns is shown in Figure 1a. The region 2θ = 7.8−8.3° (at λ = 0.413609 Å) shows the (211) and the (020) reflections for $LiCoPO_4$ and $CoPO_4$, and most clearly reveals the changes in the unit cell parameters upon cycling. Upon charging, the characteristic two-phase behavior between $LiCoPO_4$ => Li_xCoPO_4 (at 4.82 V) and Li_xCoPO_4 => $CoPO_4$ (at 4.89 V) is observed via the simultaneous disappearance and appearance of the reflections of the starting material and product, respectively. After the first charge, the Bragg reflections are broadened to the point where they are difficult to distinguish from the background. However, a small peak at $2\theta \approx 8.1°$, corresponding to the Li_xCoPO_4 phase, appears on discharge after the disappearance of the $CoPO_4$ (020) reflection, suggesting that both two-phase reactions involving the intermediate are reversible. Our results agree well with the diffraction results reported by Bramnik et al.,[15,17] as we see both a significant loss of long-range order after the first charge (shown by the decrease in intensity of the Bragg reflections) and the formation of an intermediate, Li_xCoPO_4. So-called "amorphization" has also been observed in ex situ XRD after chemical delithiation, which indicates that this behavior is intrinsic to the material and is not a consequence of interaction with the X-ray beam.[17,18] More recently, a slight loss of long-range order has also been seen for $LiFePO_4$, but the phenomenon is less pronounced than for $LiCoPO_4$.[61]

Rietveld refinements were carried out using the diffraction patterns acquired during the first charge; the scale factor of the refined phases and the unit-cell volume are shown in panels b and c in Figure 1, respectively. The analyses confirm the qualitative observation of two distinct two-phase reaction processes (indicated by a block of green crosses above the figure). However, it is surprising that there are regions, denoted by diagonal red lines above the figure, within which there is very little evidence of any reaction, i.e., there is neither the formation of a new phase, nor a significant change in the lattice parameters (a solid solution mechanism would manifest itself in the XRD patterns as a gradual change in the unit-cell parameters). Very small changes do, however, occur with respect to the peak position, which are difficult to observe owing to the accompanying broadening of the peaks; these changes are more clearly seen in Figure S3c in the Supporting Information. This suggests that small structural changes (including some partial delithiation) are required to trigger the onset of the next process. The electrochemical activity in these regions is likely dominated by side reactions, i.e. oxidation of the electrolyte,[13,14] formation of the solid electrolyte interface, and/or metal dissolution.[62] We tentatively suggest that the growth of the $CoPO_4$ phase from the intermediate phase is associated with a large activation energy, and the side-reactions compete with this structural transformation. The areas indicated with green crosses in panels b and c in Figure 1 sum to ∼160 mAh/g, suggesting that the main electrochemical reaction occurs within these regions (the theoretical capacity of $LiCoPO_4$ is 167 mAh/g). The crystalline phase fraction continues to diminish, even in regions where side reactions dominate, suggesting that the reduction in long-range order is not directly correlated with the delithiation reaction, but instead depends on the time that the cell remains at high potentials.

Overall, a very large capacity of ∼250 mAh/g is measured on the first charge. However, the discharge capacity for the first cycle is 149 mAh/g (89% of the theoretical capacity), suggesting that, while side reactions are significant (with 40% of the charge capacity being irreversible on the first cycle), Li intercalation and deintercalation in $LiCoPO_4$ is largely unaffected by them. This is the highest reversible capacity documented in the literature for this material, and is evidence that the loss of long-range order does not impact the reversibility of the reaction, at least for the first few cycles. The additional capacity associated with the side reactions at the

dx.doi.org/10.1021/cm502680w | Chem. Mater. 2014, 26, 6193−6205

beginning of charge (i.e., below 4.75 V) drops noticeably in subsequent cycles, while the additional capacity at higher voltages is still observed (see the Supporting Information). No attempt was made here to minimize the side reactions through the introduction of additives or by surface coating of electrode particles, since our focus here is on the structural transformations that occur in this system. We note that a recent XRD and NMR study of this system has shown these side reactions can be partially reduced by the use of electrolyte additives like HFiP.[43,63]

Interestingly, the volume of the $LiCoPO_4$ primitive olivine cell decreases slightly from 284.1 to 282.1 Å^3 (decrease of 0.7%) as its phase fraction decreases to zero, approaching that of the Li_xCoPO_4 phase when it first appears, at 281.4 Å^3. Similarly, the cell volume of Li_xCoPO_4 varies noticeably from 281.4 to 278.2 Å^3 (decrease of 1.1%) across its two-phase coexistence with $LiCoPO_4$, and appears to sustain a larger solid solution range than the two end members. Of particular note, the phase that forms during each of the two-phase reactions (Li_xCoPO_4 followed by $CoPO_4$) has a larger solid solution regime (i.e., a larger range in cell volume) than the phase being consumed ($LiCoPO_4$ and Li_xCoPO_4, respectively). One explanation for this is that the new phase, which nucleates and grows within the parent phase, is distorted to compensate for the difference in cell parameters and to reduce the coherency strain at the grain boundary. The greater deviation in Li composition in the nucleating phase is consistent with the work carried out by Ravnsbæk et al. on the $LiFe_xMn_{1-x}PO_4$ materials, which they attribute to a small amount of a coherently nucleating phase.[64]

There appears to be a lag between the two major plateaus observed in the galvanostatic cycling and the two-phase reaction regions emerging from the refinements, a voltage increase from 4.82 to 4.89 V being observed before the $LiCoPO_4$ phase has fully converted to Li_xCoPO_4. However, the agreement is significantly better if we compare the electrochemically active regions determined by XRD with the plateaus obtained from the open circuit voltage (OCV) within galvanostatic intermittent titration technique (GITT) experiments, as shown by black dashed lines in Figure 1d. Note that the GITT data was taken from the fourth cycle, where the "latent" (side reaction) period observed at the beginning of the charge is significantly shorter. Thus, the GITT data has been offset by 25 mAh/g in order to align the electrochemically active regions with the XRD volume changes. The overpotential increases noticeably before the end of the first plateau (with an OCV of 4.75 V), resulting in an increase in the potential measured under galvanostatic conditions from 4.82 to 4.89 V. The overpotential appears to correlate with the concentration and cell volume of the minority phase within the two-phase reaction. During the 4.75 V plateau, the overpotential is at a minimum when Li_xCoPO_4 nucleates and is the minority phase within the $LiCoPO_4$ particle. As Li_xCoPO_4 grows and $LiCoPO_4$ becomes the minority phase, the overpotential increases. The overpotential increases at the same point in the electrochemistry as the decrease in the volume of $LiCoPO_4$ from its initial value of 284.1 Å^3, the volume presumably contracting so that it can be accommodated within the Li_xCoPO_4 majority particle. The voltage associated with Li extraction will be increased by the overpotential required to drive the energetically unfavorable decrease in cell volume in $LiCoPO_4$.

To estimate the Li content in the intermediate phase, we compared the lattice parameters of the intermediate structure with those of the end members, and the Li content was obtained using Vegard's Law. On the basis of the volume of Li_xCoPO_4, a value of $x = 0.72$ is obtained. However, the a, b, and c lattice parameters considered separately would indicate a Li stoichiometry of $x = 0.80$, 0.47 and 0.66, respectively (the end member cell parameters are shown in the Supporting Information). Therefore, due to the anisotropic changes in the lattice parameters of Li_xCoPO_4, compared to those of $CoPO_4$ and $LiCoPO_4$, we are only able to provide, based on the XRD results, a range ($0.47 \leq x \leq 0.80$) within which we expect to find the Li composition of the intermediate.

NMR Spectroscopy. Ex situ ^{31}P and ^{7}Li NMR spectroscopy was carried out on $LiCoPO_4$ at different states of charge and discharge, obtained by galvanostatically cycling the battery at a rate of $C/20$ (Figure 2). The Li_xCoPO_4 intermediate is observed in the spectra of both nuclei, and is therefore deemed stable in the absence of a current.

There is again a significant delay between the start of the electrochemistry and the onset of delithiation in $LiCoPO_4$, which agrees with the XRD data and strongly indicates the

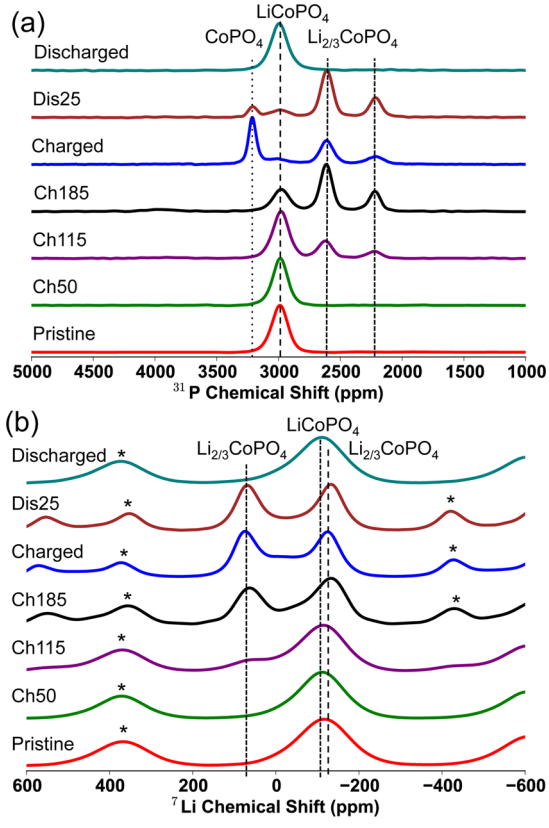

Figure 2. Ex situ (a) ^{31}P MATPASS and (b) ^{7}Li Hahn echo MAS NMR spectra recorded at a magnetic field strength of 4.7 T and at a spinning speed, ν_r, between 38 and 39 kHz, at different points in the first galvanostatic cycle of $LiCoPO_4$, cycled at a rate of $C/20$. The labels 'Ch50', "Ch115" and "Ch185" refer to the spectra of the $LiCoPO_4$-composite electrode, which has been charged up to 50, 115, and 185 mAh/g, respectively. The spectra labeled "discharged" and "Dis25", were both fully charged and subsequently either fully discharged or discharged for 3 h, respectively. All of the spectra have been normalized so that the maximum intensity is equal to 1. Spinning sidebands are marked with an asterisk.

dx.doi.org/10.1021/cm502680w | Chem. Mater. 2014, 26, 6193−6205

(a)

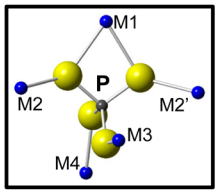

Co = blue
O = yellow
Li = orange
P = grey

(b)

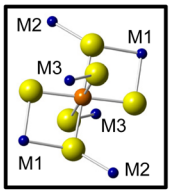

(c)

	M1	M2	M2'	M3	M4
P1	Co1	Co12	Co6	Co1	Co9
P2	Co7	Co11	Co10	Co7	Co3
P3	Co12	Co1	Co11	Co12	Co4
P4	Co2	Co9	Co5	Co2	Co6
P5	Co3	Co5	Co8	Co3	Co7
P6	Co4	Co8	Co9	Co4	Co12
P7	Co5	Co3	Co2	Co5	Co10
P8	Co8	Co4	Co3	Co8	Co11
P9	Co9	Co2	Co4	Co9	Co1
P10	Co10	Co6	Co7	Co10	Co5
P11	Co11	Co7	Co12	Co11	Co8
P12	Co6	Co10	Co1	Co6	Co2

(d)

	M1	M1	M2	M2	M3	M3
Li1	Co1	Co2	Co6	Co9	Co9	Co6
Li2	Co10	Co2	Co5	Co6	Co5	Co6
Li3	Co3	Co11	Co7	Co8	Co7	Co8
Li4	Co4	Co1	Co12	Co9	Co12	Co9
Li5	Co6	Co9	Co1	Co2	Co2	Co1
Li6	Co5	Co7	Co10	Co3	Co10	Co3
Li7	Co12	Co8	Co4	Co11	Co4	Co11
Li8	Co10	Co3	Co5	Co7	Co5	Co7
Li9	Co4	Co11	Co12	Co8	Co12	Co8
Li10	Co5	Co6	Co10	Co2	Co10	Co2
Li11	Co7	Co8	Co3	Co11	Co11	Co3
Li12	Co12	Co9	Co4	Co1	Co4	Co1

Figure 3. First coordination shell of Co atoms around (a) P and (b) Li in the olivine structure. Tables showing (c) the 12 P and (d) 12 Li sites generated in the ($a \times 3b \times c$) supercell of the olivine structure, and their nearest Co atoms. The Co atoms shaded in red and white represent Co^{3+} and Co^{2+}, respectively, generating three P and two Li local environments in the Co^{2+}/Co^{3+} arrangement shown here.

existence of side reactions in this region, the peaks from Li_xCoPO_4 only being observed after Li extraction corresponding to a capacity of 50 mAh/g. However, once commenced, the reaction apparently occurs steadily. After 185 mAh/g, the Li_xCoPO_4 peaks decrease with the growth of the $CoPO_4$ peak (this is only observable in the MATPASS ^{31}P NMR spectra, as there is a negligible contribution from Li in a "Co^{3+}" environment in $CoPO_4$). Both two-phase mechanisms are reversible on discharge: the ^{31}P $CoPO_4$ peak (δ_{iso} = 3201 ppm) decreases with the growth of the Li_xCoPO_4 peaks, which then decrease with the growth of the $LiCoPO_4$ peak. The shift and line width of the $LiCoPO_4$ ^{31}P resonance (at δ_{iso} = 2989 ppm) after one cycle is similar to that observed initially, indicating that the "amorphization" observed with in situ XRD corresponds only to a loss of long-range structure, the short-range structure being unchanged; this is consistent with the reversible electrochemistry of the $LiCoPO_4$ phase. The NMR results do not imply much compositional variation, as observed in the XRD data, specifically for the intermediate Li_xCoPO_4 phase. This must in part be due to the limited number of samples examined by using NMR spectroscopy, but may also be a result of the absence of a current in the ex situ NMR experiments, permitting solid solutions to relax into more structurally homogeneous end member phases of the reactions, so that only resonances associated with the $LiCoPO_4$, Li_xCoPO_4 and $CoPO_4$ phases are observed. Hahn-echo ^{31}P NMR spectra were also acquired for the same samples (see the Supporting Information); yielding similar shifts and intensities for the various resonances across the electrochemical range. We chose to analyze the MATPASS spectra in greater detail since these spectra do not suffer the additional complications of the overlap between the isotropic resonance of one environment and the sidebands of another. Our ^{7}Li and ^{31}P NMR spectra are essentially identical to those obtained recently in an NMR and XRD study of this material.[43]

From the NMR spectra, we are able to extract information about the local structure of the intermediate phase: two ^{31}P resonances are observed at δ_{iso} = 2610 and 2210 ppm, and two ^{7}Li resonances at δ_{iso} = 69 and −125 ppm. The ^{7}Li resonance at −125 ppm in the intermediate overlaps with the isotropic shift observed for the fully lithiated phase, suggesting that it arises from a Li nucleus predominantly surrounded by Co^{2+} ions. From the "Charged" ^{7}Li spectrum (i.e., the $LiCoPO_4$ electrode that has been fully charged to 5.0 V), where the features of the intermediate phase are most prevalent, the integrated intensity indicates that the two environments are present in an approximately 1:1 ratio (the measured ratio is 1:1.23, the higher intensity of the −125 ppm resonance being ascribed to minor contributions from the overlapping $LiCoPO_4$ resonance). The ^{31}P MATPASS "Ch185" spectrum (i.e., the point at which the $LiCoPO_4$ electrode has been charged to a capacity of 185 mAh/g) shows the clearest resolution of the ^{31}P intermediate peaks and suggests that the two P environments are present in an approximately 2:1 ratio (a value of 2:0.87 was calculated for resonances δ_{iso} = 2610 and 2210 ppm, respectively). Note that the different spin−spin (T_2) relaxation times for the two ^{31}P and two ^{7}Li environments have been accounted for in the intensity analysis (see the Supporting Information).

Although it is possible to have two ^{31}P environments that have similar isotropic shifts and that give rise to overlapping peaks in the NMR spectrum, our former studies of the $LiFe_xMn_{1-x}PO_4$ and $LiFe_xCo_{1-x}PO_4$ materials[41,65] have shown that the hyperfine shift is highly sensitive to the geometry of the transition metals around P and to the oxidation state. It is therefore unlikely for two ^{31}P environments to have the exact same shift, and, as there is no significant additional peak broadening or distortion of the more intense resonance, this suggests that the observed resonances correspond to two distinct environments occurring in a 2:1 ratio. It would be helpful to perform ^{7}Li or ^{31}P 2D homonuclear correlation experiments on the intermediate phase to obtain insight into the spatial proximities of the environments giving rise to the resonances. However, NMR simulations (see the Supporting Information) show that such experiments are extremely challenging because of the large hyperfine dipolar interactions which are much larger than the dipolar coupling between the nuclei, and the short spin−lattice (T_1) relaxation times relative

dx.doi.org/10.1021/cm502680w | Chem. Mater. 2014, 26, 6193−6205

to the time required to establish significant correlations between the different nuclei using a dipolar recoupling scheme.

Although it is surprising at first sight to observe ^{31}P NMR resonances associated with Li_xCoPO_4 lying beyond the range demarked by the end member $LiCoPO_4$ and $CoPO_4$ shifts, a similar phenomenon was observed for the P environments in $LiFe_xCo_{1-x}PO_4$, where many of the observed resonances did not fall between those of pure $LiFePO_4$ and $LiCoPO_4$.[66] This is attributed to the high degree of sensitivity of the ^{31}P hyperfine shift to the individual geometries and d-orbital occupancies of the M−O-P (M = Fe^{2+}, Co^{2+}, and Co^{3+}) bond pathways.

Intermediate Structure, Li_xCoPO_4. We now use the constraints set by the NMR spectra (in particular, the number of different P and Li local environments and their spectral weights), in combination with the lattice parameters extracted from the XRD refinements, to propose a composition and structure for the intermediate phase. The anisotropic changes of the lattice parameters of the intermediate with respect to the unit-cell parameters of the end members led us to consider a range of intermediate phase compositions, i.e., $Li_{0.47-0.80}CoPO_4$. It is not possible to devise a Li and Co^{2+}/Co^{3+} ordering scheme within the original olivine unit-cell that gives rise to two different ^{31}P resonances with a 2:1 intensity ratio, since this cell contains four P atoms. Therefore, a reasonable first assumption is that the intermediate structure is represented by an expansion of the original olivine primitive cell. In order to analyze the different possible structures in a systematic way, we proceed by considering the following supercell expansions: $(2a \times b \times c)$, $(a \times 2b \times c)$, $(a \times b \times 2c)$, $(3a \times b \times c)$, $(a \times 3b \times c)$, and $(a \times b \times 3c)$ (i.e., three cells are doubled and three cells are tripled along either the *a*, *b*, and *c* axes) to create six supercells. We also consider a seventh expansion, the $Na_{2/3}FePO_4$ superstructure,[23,28] which formally involves cell tripling in two directions, (either $(3a \times 3b \times c)$[23] or $(a-b \times 3b \times c)$[28]).

Because the ^{31}P Fermi contact shifts are much more sensitive to the nature and/or oxidation state of the transition metals in the first coordination shell than the ^{7}Li NMR spectra,[41,65] we first analyze the ^{31}P spectra before proceeding to examine the Li environments. There are five Co positions (labeled M1, M2, M2′, M3, and M4 in Figure 3a) in the first cation coordination shell of P in the olivine structure, of which two are equivalent (M2 and M2′) because of the presence of a mirror plane passing through the P atoms in the pure $LiMPO_4$ and MPO_4 phases.[65] Seven tables were created (see the Supporting Information) with the 8, 12, and 12 P local sites (from cell doubling, tripling, and the $(a-b \times 3b \times c)$ supercell, respectively) and the five different (labeled) Co atoms in the first coordination shell around the P sites. In these supercells, the periodicity imposes further limits on the possible range of P environments; e.g., in the $(2a \times b \times c)$ supercell, P1 is surrounded by two Co1 atoms from two different cells on the M1 and M3 positions, two Co5 atoms from two cells on M2 and M2′ and a Co6 atom on M4.

All configurations obtained when the cell is doubled were immediately dismissed because there are 8 P atoms in the supercell, so it is never possible to obtain two ^{31}P sites in a 2:1 ratio. We then considered the different cells (and different P local environments) generated by assuming that the different Co sites were either Co^{2+} or Co^{3+}, in the appropriate ratios to form Li compositions falling within the range $Li_{0.47-0.80}CoPO_4$.

When the unit cell is tripled along either the *a*, *b*, or *c* axis, every arrangement of Co^{2+} and Co^{3+} ions generates more than two ^{31}P sites, in disagreement with the ^{31}P NMR experimental data (illustrated in Figure S7d−i in the Supporting Information). After a thorough analysis in which all possible combinations were explored, the closest agreement with the NMR data was achieved with a Co^{2+} to Co^{3+} ratio of 2:1, resulting in three different P environments in a 1:1:1 ratio (Figure S7d, f in the Supporting Information). When the cell is tripled along the *b*-direction, however, two of these three P environments consist of one Co^{3+} on either the M2 or the M2′ site, and four Co^{2+} on the remaining sites (P1, P2, P4, P5, P8, P9, P11, and P12 in Figure 3c). Because the mirror plane on P is retained in the cosubstituted materials, $LiFe_xMn_{1-x}PO_4$ and $LiFe_xCo_{1-x}PO_4$, it strongly suggests that in Li_xCoPO_4, M2 and M2′ are also equivalent. The bond lengths and bond angles generated by our calculations support this assumption, as discussed in the DFT study. Therefore, even though three P environments arise, two of them are expected to give rise to identical shifts in the presence of the mirror plane, resulting in two peaks occurring in a 2:1 ratio.

There are three symmetrically equivalent possible combinations of Co^{2+}/Co^{3+} ordering for the $(a \times 3b \times c)$ superstructure. They can be superimposed onto each other by a translation in the direction perpendicular to the Co chains (see the Supporting Information), which, as observed in Figure 3d, results in a total of two distinct Li environments: four Li sites surrounded by six Co^{2+} (denoted Li*α*, Figure 4d) and

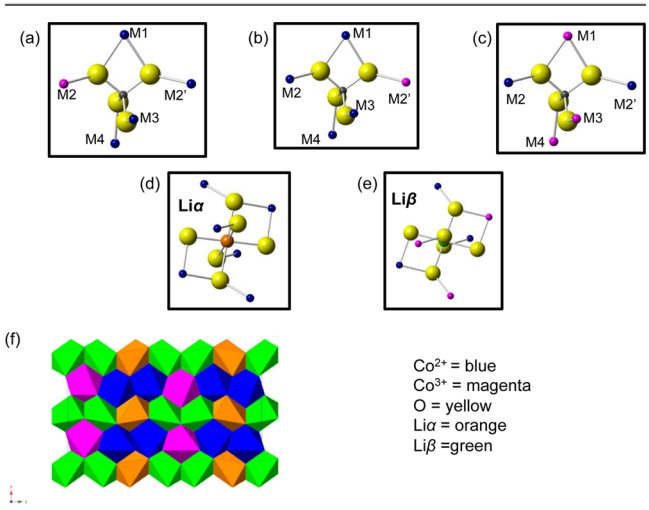

Figure 4. (a−c) Three P environments (present in a 1:1:1 ratio) and (d, e) two Li environments (which are present in a 1:1 ratio) in the $Li_{2/3}CoPO_4$ structure. Because M2 = M2′, a and b are equivalent. (f) There are 8 Li*β* sites (shown in green), 4 of which must be removed for charge balancing (Co^{2+}, Co^{3+} and Li*α* are shown in blue, magenta, and orange, respectively).

eight Li sites surrounded by three Co^{2+} and three Co^{3+} (denoted Li*β*, Figure 4e). Li*α* is assigned to the ^{7}Li resonance at −125 ppm, as it overlaps with the pristine ^{7}Li resonance (i.e., Li surrounded by 6 Co^{2+} ions). The composition $Li_{2/3}CoPO_4$ implies that four Li ions must be removed from the supercell. Given the experimentally observed intensities, the Li ions must be removed from the Li*β* sublattice, yielding two Li environments in a 1:1 ratio, in agreement with the ^{7}Li NMR results. The proposed Li environments are shown in Figure 4f. Note that this differs from the ordering scheme proposed in the recent ^{7}Li and ^{31}P NMR study.[43]

The $(a-b \times 3b \times c)$ supercell present in the $Na_{2/3}FePO_4$[23,28] intermediate structure was explored, and the same Fe^{2+}/Fe^{3+}

dx.doi.org/10.1021/cm502680w | Chem. Mater. 2014, 26, 6193−6205

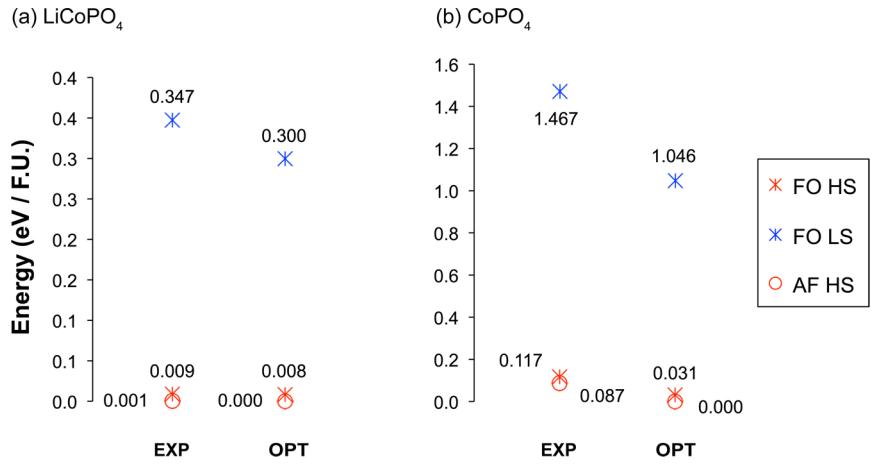

Figure 5. Energy diagrams of (a) $LiCoPO_4$ and (b) $CoPO_4$ in their experimental (EXP)[16] and DFT optimized (OPT) structures, within the GGA +U (U_{eff} = 5.48 eV) approach. Total energies were calculated for cells in which all Co spins were ferromagnetically (FO) aligned (in either their low (LS) or high (HS) spin state), and on cells in which the HS Co spins were antiferromagnetically (AF) aligned, as reported in a previous magnetic study on these phases.[16]

ordering observed in both these studies was implemented for Co^{2+}/Co^{3+} (Figure S8 in the Supporting Information). However, this ordering results in five different P sites. When M2 and M2′ are assumed to be equivalent, three distinct ^{31}P environments are predicted in a 1:1:1 ratio, which still disagrees with the ^{31}P NMR data. The $(a \times b \times 3c)$ supercell, which was recently suggested by Kaus et al.[43] for the $Li_{2/3}CoPO_4$ intermediate, is presented in Figure S7d in the Supporting Information and results in the presence of five inequivalent ^{31}P environments in a 2:1:1:1:1 ratio, so it is not considered further.

First-Principles Calculations. First-principles DFT calculations were performed on the end member phases and on the proposed $Li_{2/3}CoPO_4$ intermediate structure to determine the lowest-energy spin state and magnetic alignment at all three stages of charge of the $LiCoPO_4$ electrode. The calculations considered both structures with fixed experimental cell parameters and atomic positions, as obtained from Rietveld refinement of neutron and XRD data,[16] and fully optimized structures. The relative stability of different Li^+/vacancy ordering schemes in the intermediate was also explored.

Ab Initio Investigation of the Relative Stability of Different Spin States and Magnetic Alignments in the End Member Compounds. The calculations on $LiCoPO_4$ and $CoPO_4$ were performed using an average U_{eff} value of 5.48 eV, as derived for the mixed valence $Li_{2/3}CoPO_4$ system. A high spin ground state was predicted for both end member phases, in agreement with previous experimental[16] and theoretical studies.[29] The previous DFT study reported that different magnetic ordering schemes of the transition metal ions lead to energy differences of 10−60 meV per formula unit.[29] Our results on the $LiCoPO_4$ and $CoPO_4$ end member phases, presented in the two diagrams in panels a and b in Figure 5, show that these energy differences can be orders of magnitude larger when the different spin states of the Co^{2+} and Co^{3+} atoms are also considered, a result in line with the fact that intraatomic exchange interactions are typically a few electron volts, whereas interatomic exchange interactions are in the millielectron volt range.

Only one antiferromagnetic state is reported here for $LiCoPO_4$, as the antiferromagnetic low-spin cells converged to the high-spin state upon release of magnetic constraints. The total energies of the high spin ferromagnetic and antiferromagnetic $LiCoPO_4$ states differ by 8 meV per formula unit in both the experimental and optimized structures. As expected, the low-spin state is highly unfavorable and lies more than 300 meV per formula unit above the high-spin ground state.

In the DFT calculations performed on the $CoPO_4$ structure, all cells with the Co^{3+} spins initialized in the intermediate-spin state converged to high-spin states and are therefore not represented in Figure 5b. The high-spin antiferromagnetic ground state lies at ca. 30 meV per formula unit below the high spin ferromagnetic state. Again, the low-spin state is much higher in energy, by more than 1 eV per formula unit.

In summary, our calculations confirm the antiferromagnetic ground state and spin alignment deduced experimentally, for both $LiCoPO_4$ and $CoPO_4$ structures, by Ehrenberg et al.[16] This study on the end member compounds yields results in good agreement with previous experimental[16,32] and theoretical[29] studies, and can now be used to determine the relative stabilities of the different (Li and magnetic) configurations considered here as potential $Li_{2/3}CoPO_4$ intermediate phases.

DFT Investigation of the Relative Stability of Different Spin States and Magnetic Alignments in the $Li_{2/3}CoPO_4$ Intermediate Structures. As previously described, the ^{31}P NMR data for the intermediate phase $Li_{2/3}CoPO_4$ suggest a tripling of the $LiCoPO_4$ unit cell along the *b*-direction. The site occupation disorder (SOD) code,[67] devised to determine a minimal set of symmetry-unique configurations for site-disorder problems in solids, was used with the *Pnma* $LiCoPO_4$ unit cell as the input structure. The $(a \times 3b \times c)$ supercell (Figure 4f) was created. It contains 12 Li atoms, four of which were systematically removed by the SOD code in order to generate all possible structures with a $Li_{2/3}$ stoichiometry. The code generated thirty-two symmetry inequivalent supercells, in which all the Co sites were assumed to be equivalent. Co^{3+}/Co^{2+} ordering along the *b*-direction, identified on the basis of the ^{31}P experimental NMR data, was implemented for each of the thirty-two possible Li configurations. Nineteen of these structures were discarded, as they did not agree with the ^7Li NMR data (i.e., they involved the removal of one or more Li^+ ion(s) from the Liα sublattice). Close examination of the 13 remaining structures lead us to reject a further seven of them that had either triple or higher aggregates of Li vacancies close

dx.doi.org/10.1021/cm502680w | *Chem. Mater.* 2014, 26, 6193−6205

to each other, and/or a highly anisotropic charge distribution. The final six configurations (a–f) are shown in Figure 6.

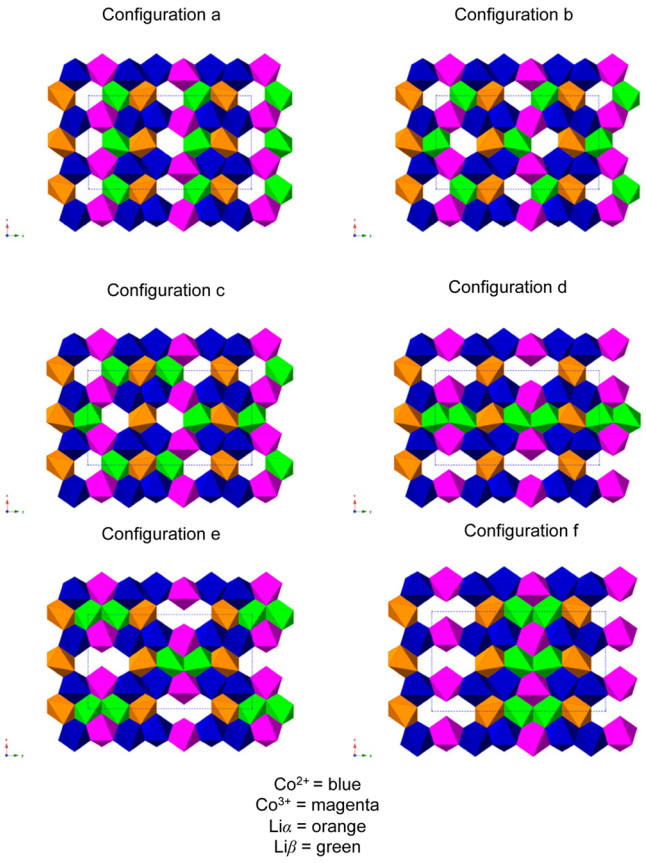

Figure 6. Six different Li^+/vacancy ordering schemes on which DFT calculations were performed, which are all consistent with the experimental ^7Li and ^{31}P NMR and XRD data. Co^{2+} and Co^{3+} are shown in blue and magenta, respectively, and Liα and Liβ are shown in orange and green, respectively.

The energies of the most stable (antiferromagnetic high spin) configurations for the end member structures optimized ab initio were used to calculate the formation energies of the six different Li^+/vacancy configurations. A Li_xCoPO_4 convex hull was generated (presented in Figure S10 in the Supporting Information), which includes the energy of all the (intermediate and high) spin states, and magnetic configurations (ferromagnetic, antiferromagnetic) which reached electronic convergence without spin constraints in the last single-point energy DFT calculation. Additionally, the formation energies of all of the $LiCoPO_4$, $Li_{2/3}CoPO_4$, and $CoPO_4$ spin and magnetic configurations investigated in this study are summarized in Table S2 in the Supporting Information. The Li_xCoPO_4 convex hull presented in Figure 7 only shows the lowest energy spin and magnetic state, for each of the six different Li configurations considered within the pure GGA and GGA+U (U_{eff} = 5.48 eV) approaches. We will analyze the GGA+U results in this section, then comment on the insight into the mechanisms stabilizing the $Li_{2/3}CoPO_4$ intermediate obtained from the GGA results in the Discussion section. Within GGA +U, apart from configuration b, none of the Li arrangements considered for the $Li_{2/3}CoPO_4$ structure are stable in the intermediate-spin state. The (ferromagnetically and antiferromagnetically coupled) intermediate-spin state either does not reach electronic convergence in the absence of magnetic constraints, or converges to the high-spin state when the magnetic constraints are released. Configuration b is the only exception to the rule: its ferromagnetic high-spin state is not stable and converges to the ferromagnetic intermediate-spin state in the absence of constraints on the Co spins. Moreover, this ferromagnetic intermediate-spin state is found to be the lowest-energy spin state for this configuration, and the second lowest energy configuration out of all the Li configurations investigated in this study.

Figure 7 and Figure S10 and Table S2 in the Supporting Information clearly demonstrate that all of the $Li_{2/3}CoPO_4$ configurations tested in this study are thermodynamically stable with respect to the two end member phases. The lowest energy configuration observed in Figure 7 (configuration a in the antiferromagnetic high spin state) has a negative formation energy of 309 meV per formula unit. A map of the spin density of this configuration is presented in Table S2 in the Supporting Information. All Li configurations considered in Figure 7 lie within an energy range of ca. 84 meV per formula unit. The formation energies of the three most stable configurations (Figure 6a–c) differ by less than 5 meV per formula unit, and we may expect more than one structure to be present at room temperature. These three low energy configurations (a, b and c) have minimal differences in the arrangement of the Li vacancies, and can be interconverted by Li ion hops to adjacent Liβ sites. It is likely that the intermediate structure contains a disordered Li sublattice comprising all of these different Li local environments. Configurations d–f contain vacancies arranged in pairs, which were shown in calculations on $Li_{0.6}FePO_4$ materials to be the most energetically favorable configurations.[21]

As previously discussed, the experimental observation of only two ^{31}P resonances implies an equivalence of the M2 and M2′ metal positions in the first P coordination shell. To determine whether this equivalence is observed computationally, we compared the $Co^{3+/2+}$ (M2)–O–P and $Co^{3+/2+}$(M2′)–O–P bond pathway geometries, in the lowest-energy $Li_{2/3}CoPO_4$ supercell optimized ab initio (configuration a in the high-spin antiferromagnetic state). No differences are observed between the Co–O and O–P bond lengths and the Co–O–P bond angles involving either M2 or M2′ (i.e., the mirror plane is preserved), helping to validate our assertion that only two ^{31}P local environments are present.

DISCUSSION

The excellent agreement between the number of distinct Li and P local environments and their relative populations, predicted using the model outlined above and the experimental ^7Li and ^{31}P NMR data obtained for the intermediate structure, led us to propose an intermediate phase with stoichiometry $Li_{2/3}(Co^{2+})_{2/3}(Co^{3+})_{1/3}PO_4$, and with a superstructure obtained by tripling the unit cell in the *b*-direction. This result should be contrasted to previous structural reports for other $A_{2/3}$ polyanionic intermediates (A = Li, Na), $Li_{2/3}VPO_4F$ and $A_{2/3}FePO_4$.[27,68] Although a $Li_{2/3}VPO_4F$ intermediate has been identified when $LiVPO_4F$ is electrochemically charged, the crystal structure is still unknown. The $A_{2/3}FePO_4$ and $Li_{2/3}CoPO_4$ intermediates adopt different superstructures with the former consisting of a tripling in both the *b*- and *a*-directions (Figure S8). Three inequivalent sites are generated from this superstructure, in disagreement with the experimental observations for $Li_{2/3}CoPO_4$. Interestingly, we observed two

dx.doi.org/10.1021/cm502680w | *Chem. Mater.* 2014, 26, 6193–6205

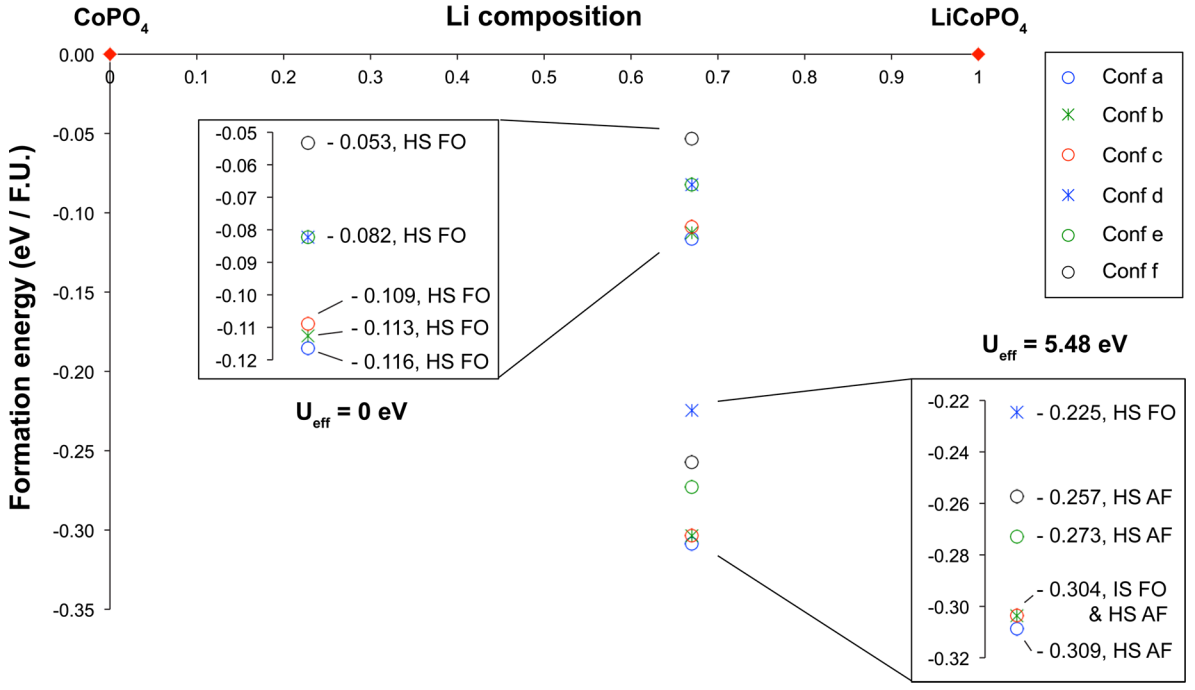

Figure 7. Convex hull for Li_xCoPO_4, calculated within the GGA (U_{eff} = 0 eV) and GGA+U (U_{eff} = 5.48 eV) approaches. The formation energies of the different Li_xCoPO_4 (x = 0, 2/3, 1) phases are plotted against Li composition, in eV per formula unit (eV/F.U.). The insets show the −0.32 to −0.22 eV/F.U. and the −0.12 to −0.05 eV/F.U. regions of the convex hull, corresponding to the range of formation energies of the $Li_{2/3}CoPO_4$ intermediate structures in GGA+U and in GGA, respectively. Although GGA calculations were only performed in the ferromagnetically aligned state, GGA+U calculations were performed in the ferromagnetically and antiferromagnetically aligned states. Only the lowest energy spin and magnetic state, for each of the different $Li_{2/3}CoPO_4$ Li arrangements investigated, is plotted. Table S2 in the Supporting Information summarizes the outcome of all calculations performed on the $Li_{2/3}CoPO_4$ cells, in GGA and in GGA+U. IS, HS, FO and AF denote the intermediate spin state, the high spin state and the ferromagnetically and the antiferromagnetically aligned phases, respectively.

^{31}P resonances in our previous studies of $Li_{2/3}FePO_4$ obtained by cooling micron-sized particles of chemically delithiated $LiFePO_4$, suggesting that more than one superstructure may exist for $Li_{2/3}FePO_4$.[69] The absence of superlattice reflections in the in situ XRD data shown here was accounted for by performing simulations of the $Li_{2/3}CoPO_4$ diffraction pattern. The simulations show that the intensity of the superlattice reflections are 1/100th of that of the main Bragg peaks (see the Supporting Information), and are not observable because of the significant broadening of the peaks; further TEM analyses are ongoing.

Our calculations predict that all six $Li_{2/3}CoPO_4$ intermediate configurations investigated here lie below the $LiCoPO_4$–$CoPO_4$ convex hull, conversely to the $Li_{2/3}FePO_4$ case, for which the intermediate is only metastable and lies above the $LiFePO_4$–$FePO_4$ convex hull.[28,70] Therefore, in the Co system, the thermodynamics will drive the formation of the intermediate phase. The activation energy barrier associated with the structural transformations will also be lowered over that involving the direct delithiation of $LiCoPO_4$ to form $CoPO_4$, since the intermediate phase is able to buffer the volume changes associated with delithiation. The relative changes in the sizes of the *a*, *b*, and *c* unit-cell parameters, and subsequent changes in the areas of the ab, ac and bc faces of the unit cell (Table 1), allow us to speculate on a possible orientation of any interface between $LiCoPO_4$ and $Li_{2/3}CoPO_4$ and between $Li_{2/3}CoPO_4$ and $CoPO_4$ within a reacting particle. For the $LiCoPO_4$ => $Li_{2/3}CoPO_4$ and $Li_{2/3}CoPO_4$ => $CoPO_4$ reactions, the changes in the area of the bc cell faces are 0.7% and 0.1%, respectively. These changes are minor in comparison

Table 1. Percentage Changes in the Unit-Cell Parameters, in the Areas of the *ab*, *ac*, and *bc* Faces of the Unit Cell, and in the Cell Volumes for the Two Reactions $LiCoPO_4$ => $Li_{2/3}CoPO_4$ and $Li_{2/3}CoPO_4$ => $CoPO_4$[a]

	%						
	Δ*a*	Δ*b*	Δ*c*	Δ*ab*	Δ*ac*	Δ*bc*	Δvolume
$LiCoPO_4$ - $Li_{2/3}CoPO_4$	1.2	1.2	−0.4	2.4	0.8	0.7	2.0
$Li_{2/3}CoPO_4$ – $CoPO_4$	5.1	1.1	−0.9	6.1	4.2	0.2	5.3

[a]The changes are calculated relative to the $LiCoPO_4$ and $Li_{2/3}CoPO_4$ structures, respectively.

to the changes of 2.4% and 6.1% in the area of the ac cell faces for the $LiCoPO_4$ => $Li_{2/3}CoPO_4$ and $Li_{2/3}CoPO_4$ => $CoPO_4$ reactions, respectively. The latter being largely a result of the large change in the *a*-parameter during this reaction. These results strongly suggest that any interface between $LiCoPO_4$ and $Li_{2/3}CoPO_4$, and between $Li_{2/3}CoPO_4$ and $CoPO_4$, that forms during the electrochemical reaction, is in the *bc*-plane, in agreement with the work by Ravnsbæk et al. on $LiFe_xMn_{1-x}PO_4$.[64] Although coherency strain energy calculations have been carried out by Van der Ven[71] and Cogswell[72] on the $LiFePO_4$ system, it is not trivial to rationalize the additional stabilization of the intermediate phase in the $LiCoPO_4$ and $CoPO_4$ particles.

Ab initio calculations on the $Li_{2/3}CoPO_4$ intermediate predict its thermodynamic stability with respect to the disproportionation reaction leading to the formation of $LiCoPO_4$ and $CoPO_4$, in good agreement with experimental observations of a

dx.doi.org/10.1021/cm502680w | *Chem. Mater.* 2014, 26, 6193−6205

stable $Li_{2/3}CoPO_4$ intermediate phase in the absence of a current. These observations should be contrasted with mechanisms proposed for $LiFePO_4$ nanoparticles, where the $LiFePO_4$−$FePO_4$ interface was suggested to be unstable and the delithiation reaction to occur particle-by-particle, as proposed by the domino-cascade model.[73] Our recent results[74] and those of Zhang et al.[75] have suggested, in agreement with prior theoretical predictions,[70] that nanoparticles of $LiFePO_4$ react via a solid-solution mechanism rather than by forming an abrupt interface between the two end-member phases, at least at very high rates.

$LiCoPO_4$, $Li_{2/3}CoPO_4$, and $CoPO_4$ also show considerable variations in cell parameters from their equilibrium values during the in situ XRD measurement. This phenomenon is most pronounced when the phases exist as minority phases within the electrode (see Figure S13 in the Supporting Information). For example, the *b*-parameter of $Li_{2/3}CoPO_4$ approaches that of $LiCoPO_4$ in the initial stages of delithiation. This indicates that a substantial fraction of the particles within the electrode undergo electrochemical reaction simultaneously, in contrast to results obtained at low cycling rates for $LiFePO_4$. Thus, this system does not react particle-by-particle (the domino-cascade model). The mechanism observed here for $LiCoPO_4$ is related to the solid-solution mechanism, but is subtly different. Both mechanisms originate from the coherency strain between end-member phases. Here, the $Li_{2/3}CoPO_4$ phase must be able to accommodate a wide range of nonstoichiometry during the reaction (resulting in structural flexibility/elasticity) so that when it first forms within the $LiCoPO_4$ phase it contains excess lithium (i.e., $Li_{2/3+\delta}CoPO_4$). Because little evidence for nonstoichiometry is observed in the ex situ ^{31}P NMR experiments, we suggest that these are also metastable solid solutions, but further calculations to determine the energetics of different compositions within this system are required to investigate this phenomenon in greater depth.

Nevertheless, the DFT calculations performed in this study provide insight into the mechanisms stabilizing the $Li_{2/3}CoPO_4$ phase. The U Hubbard term in GGA+U allows charges to be localized onto particular ions of mixed-valence systems, while pure GGA results in delocalization of charge over all metal atoms. The ab initio study by Zhou et al.[76] on the Li_xFePO_4 system showed that the electronic configurational entropy needed to be taken into account to produce an accurate model for the $LiFePO_4$-$FePO_4$ phase diagram and to reproduce the eutectic point at approximately $x = 0.5$. This electronic entropy, arising due to the tendency to form distinct Fe^{2+} and Fe^{3+} oxidation states in the GGA+U calculations and their subsequent arrangements, was found to be larger than the configurational entropy associated with the distribution of Li^+ ions and vacancies in the lattice. In our work, the $Li_{2/3}CoPO_4$ formation energies obtained within the GGA approach are not as large as those calculated in the GGA+U case, the additional stability of the intermediate configurations observed in GGA+U arising from an electronic term related to localizing the charges in the structure. However, we note that the failure of pure DFT is not as severe in the case of $Li_{2/3}CoPO_4$, where the method still predicts the intermediate configurations to be below the convex hull. In contrast, in Li_xFePO_4, LDA and GGA do not predict the experimentally observed phase separation at low *T*.[77] This result is in agreement with previous GGA studies on the $LiCoPO_4$/$CoPO_4$ system.[78,79] Finally, the formation energies obtained within the pure GGA approach on the different $Li_{2/3}CoPO_4$ structures reveal that configurations a, b, and c, are lower in energy than configurations d, e and f, whether or not a U correction is applied. This suggests that the greater stabilization of configurations with single Li vacancies (a, b, and c), compared to configurations containing pairs of Li vacancies (d, e, and f), is due to more favorable electrostatics, in contrast to what has been observed for $Li_{0.6}FePO_4$.[21]

■ CONCLUSIONS

Both XRD and NMR studies show that the electrochemical delithiation reaction of $LiCoPO_4$ involves two distinct two-phase mechanisms, namely $LiCoPO_4$ => $Li_{2/3}CoPO_4$ and $Li_{2/3}CoPO_4$ => $CoPO_4$, both of which are reversible upon discharge. $Li_{2/3}CoPO_4$ is stable in the absence of a current, a result confirmed by DFT calculations of the energetics of this phase. The ex situ NMR spectra of a range of delithiated samples provide direct insight into the P and Li local environments occurring in the intermediate phase: two Li environments are present in a 1:1 ratio (one environment containing a first coordination shell of only Co^{2+} cations), along with two P environments in a 2:1 ratio. A thorough analysis of these NMR spectra led to the conclusion that the intermediate has the composition $Li_{2/3}CoPO_4$, with Co^{3+}/Co^{2+} ordering along the *b*-axis. The DFT calculations indicate that the lowest energy Li^+/vacancy ordering also occurs along the *b*-axis, with the vacancies residing next to the Co^{3+} ions. Three low energy Li^+/vacancy ordering schemes, all at ca. 300 meV below the $LiCoPO_4$−$CoPO_4$ convex hull, are identified. Their total energies lie within a range of 5 meV per formula unit, and the three configurations only differ by single Li^+ displacements between neighboring Liβ sites in the *b*-direction, in keeping with the fact that there is only a 50% occupancy of the sites neighboring both Co^{3+} and Co^{2+} ions. Thus, it is very likely that the intermediate phase contains a degree of disorder on the Li sublattice. A comparison of the formation energies obtained in GGA+U and GGA on the different $Li_{2/3}CoPO_4$ intermediate configurations reveals that an electronic term contributes to the stability of the intermediate phase.

■ ASSOCIATED CONTENT

Supporting Information

Additional information on computational methods, $LiCoPO_4$ impurity analysis during the solid-state synthesis, XRD, ^{31}P NMR and ^7Li NMR of $LiCoPO_4$, electrochemistry for the in situ XRD, the first two electrochemical cycles of $LiCoPO_4$, overlaid to demonstrate the reduction in the side reactions at the start, the unit-cell parameters of the end member phases ($LiCoPO_4$, Li_xCoPO_4 and $CoPO_4$), ex situ ^{31}P and ^7Li Hahn echo NMR spectra of Li_xCoPO_4 during the first electrochemical cycle and the points on the electrochemical curve at which ex situ NMR data was obtained, NMR homonuclear recoupling spin dynamics simulations, P environments in Li_xCoPO_4 when the primitive olivine unit cell has the following expansions: $(2a \times b \times c)$, $(a \times 2b \times c)$, $(a \times b \times 2c)$, $(3a \times b \times c)$, $(a \times 3b \times c)$, $(a \times b \times 3c)$, and $(a-b \times 3b \times c)$, the three possible Co^{2+}/Co^{3+} ordering schemes giving rise to the observed NMR data, the convex hull for Li_xCoPO_4, GITT of $LiFePO_4$ and $LiCoPO_4$, the superlattice reflections predicted for $Li_{2/3}CoPO_4$, the changes in the *a*, *b*, and *c* lattice parameters during the first charge of $LiCoPO_4$, a table summarizing the outcome of all DFT calculations performed on the Li_xCoPO_4 ($x = 0$, 2/3, 1) phases and a spin density map of the lowest energy $Li_{2/3}CoPO_4$ configuration obtained in GGA+U. This

material is available free of charge via the Internet at http://pubs.acs.org.

AUTHOR INFORMATION

Corresponding Author

*E-mail: cpg27@cam.ac.uk.

Present Address

[§]D.S.M. is currently at Department of Chemistry, University of Warwick, Gibbet Hill, Coventry CV4 7AL, United Kingdom

Author Contributions

[†]F.C.S. and R.J.C contributed equally. The manuscript was written through contributions of all authors.

Notes

The authors declare no competing financial interest.

ACKNOWLEDGMENTS

We thank the EPSRC for a Doctoral Training Partnership Award (support to FCS) and the Department of Energy (DOE) for support via the Northeastern Center for Chemical Energy Storage, an Energy Frontier Research Center funded by the U.S. Department of Energy, Office of Science, Office of Basic Energy Sciences under Award Number DE-SC0001294 (FCS, CPG, OJB, KMW, KWC, PJC). We thank the EU for financial support via an EU-ERC Advanced Fellowship (RJC) and a Marie Curie intra-European fellowship (ML). Work done at Argonne and use of the Advanced Photon Source (APS), an Office of Science User Facility operated for the U.S. Department of Energy Office of Science by Argonne National Laboratory, were supported by the U.S. Department of Energy under Contract No. DE-AC02-06CH11357. An allocation of time upon the NANO computer cluster at the Center for Functional Nanomaterials, Brookhaven National Laboratory, U.S.A., which is supported by the U.S. DOE, Office of Basic Energy Sciences, under Contract DE-AC02-98CH10886, is acknowledged. This work used the ARCHER UK National Supercomputing Service (http://www.archer.ac.uk). We thank Hao Liu, Xiao Hua, Ieuan Seymour, Dr. Phoebe Allan and Dr. Sylvia Britto for their help and discussions, Dr. Matthew Suchomel for instrument support, and Dr. Jan Ilavsky for help with the Irena software.

REFERENCES

(1) Padhi, A. K.; Nanjundaswamy, K. S.; Goodenough, J. B. *J. Electrochem. Soc.* **1997**, *144*, 1188−1194.

(2) Gibot, P.; Casas-Cabanas, M.; Laffont, L.; Levasseur, S.; Carlach, P.; Hamelet, S.; Tarascon, J.-M.; Masquelier, C. *Nat. Mater.* **2008**, *7*, 741−747.

(3) Mizushima, K.; Jones, P. C.; Wiseman, P. J.; Goodenough, J. B. *Mater. Res. Bull.* **1980**, *15*, 783−789.

(4) Zhou, F.; Cococcioni, M.; Kang, K.; Ceder, G. *Electrochem. Commun.* **2004**, *6*, 1144−1148.

(5) Okada, S.; Sawa, S.; Egashire, M.; Yamaki, J.-I.; Tabuchi, M.; Kageyama, H.; Konishi, T.; Yoshino, A. *J. Power Sources* **2001**, *97*−*98*, 430−432.

(6) Yang, J.; Xu, J. J. *J. Electrochem. Soc.* **2006**, *153*, A716.

(7) Wolfenstine, J.; Allen, J. *J. Power Sources* **2005**, *142*, 389−390.

(8) Rommel, S. M.; Schall, N.; Brünig, C.; Weihrich, R. *Monatsh. Chem.* **2014**, *145*, 385−404.

(9) Johannes, M. D.; Hoang, K.; Allen, J. L.; Gaskell, K. *Phys. Rev. B* **2012**, *85*, 115106.

(10) Wolfenstine, J.; Lee, U.; Poese, B.; Allen, J. L. *J. Power Sources* **2005**, *144*, 226−230.

(11) Yonemura, M.; Yamada, A.; Takei, Y.; Sonoyama, N.; Kanno, R. *J. Electrochem. Soc.* **2004**, *151*, A1352.

(12) Prabu, M.; Selvasekarapandian, S.; Kulkarni, A. R.; Karthikeyan, S.; Hirankumar, G.; Sanjeeviraja, C. *Ionics* **2011**, *17*, 201−207.

(13) Tarascon, J. M.; Guyomard, D. *Solid State Ionics* **1994**, *69*, 293−305.

(14) Guyomard, D.; Tarascon, J. M. *J. Power Sources* **1995**, *54*, 92−98.

(15) Bramnik, N. N.; Nikolowski, K.; Baehtz, C.; Bramnik, K. G.; Ehrenberg, H. *Chem. Mater.* **2007**, *19*, 908−915.

(16) Ehrenberg, H.; Bramnik, N. N.; Senyshyn, A.; Fuess, H. *Solid State Sci.* **2009**, *11*, 18−23.

(17) Bramnik, N. N.; Bramnik, K. G.; Buhrmester, T.; Baehtz, C.; Ehrenberg, H.; Fuess, H. *J. Solid State Electrochem.* **2004**, *8*, 558−564.

(18) Wolfenstine, J.; Poese, B.; Allen, J. L. *J. Power Sources* **2004**, *138*, 281−282.

(19) Delacourt, C.; Poizot, P.; Tarascon, J.-M.; Masquelier, C. *Nat. Mater.* **2005**, *4*, 254−260.

(20) Chen, G.; Song, X.; Richardson, T. J. *J. Electrochem. Soc.* **2007**, *154*, A627.

(21) Furutsuki, S.; Chung, S.-C.; Nishimura, S.-I.; Kudo, Y.; Yamashita, K.; Yamada, A. *J. Phys. Chem. C* **2012**, *116*, 15259−15264.

(22) Orikasa, Y.; Maeda, T.; Koyama, Y.; Murayama, H.; Fukuda, K.; Tanida, H.; Arai, H.; Matsubara, E.; Uchimoto, Y.; Ogumi, Z. *J. Am. Chem. Soc.* **2013**, 130408113515002.

(23) Galceran, M.; Saurel, D.; Acebedo, B.; Roddatis, V. V.; Martin, E.; Rojo, T.; Casas-Cabanas, M. *Phys. Chem. Chem. Phys.* **2014**, *16*, 8837.

(24) Mba, J. M. A.; Croguennec, L.; Basir, N. I.; Barker, J.; Masquelier, C. *J. Electrochem. Soc.* **2012**, *159*, A1171−A1175.

(25) Casas-Cabanas, M.; Roddatis, V. V.; Saurel, D.; Kubiak, P.; Carretero-González, J.; Palomares, V.; Serras, P.; Rojo, T. *J. Mater. Chem.* **2012**, *22*, 17421.

(26) Galceran, M.; Roddatis, V.; Zúñiga, F. J.; Pérez-Mato, J. M.; Acebedo, B.; Arenal, R.; Peral, I.; Rojo, T.; Casas-Cabanas, M. *Chem. Mater.* **2014**, 140509132811002.

(27) Lu, J.; Chung, S.-C.; Nishimura, S.-I.; Yamada, A. *Chem. Mater.* **2013**, *25*, 4557−4565.

(28) Boucher, F.; Gaubicher, J.; Cuisinier, M.; Guyomard, D.; Moreau, P. *J. Am. Chem. Soc.* **2014**, 140530160416006.

(29) Zhou, F.; Cococcioni, M.; Marianetti, C.; Morgan, D.; Ceder, G. *Phys. Rev. B* **2004**, *70*, 235121.

(30) Qian, D.; Hinuma, Y.; Chen, H.; Du, L.-S.; Carroll, K. J.; Ceder, G.; Grey, C. P.; Meng, Y. S. *J. Am. Chem. Soc.* **2012**, *134*, 6096−6099.

(31) Levasseur, S.; Ménétrier, M.; Shao-Horn, Y.; Gautier, L.; Audemer, A.; Demazeau, G.; Largeteau, A.; Delmas, C. *Chem. Mater.* **2003**, *15*, 348−354.

(32) Santoro, R. P.; Segal, D. J.; Newnham, R. E. *J. Phys. Chem. Solids* **1966**, *27*, 1192−1193.

(33) Yang, X. Q.; Sun, X.; Lee, S. J.; McBreen, J.; Mukerjee, S.; Daroux, M. L.; Xing, X. K. *Electrochem. Solid-State Lett.* **1999**, *2*, 157−160.

(34) Morcrette, M.; Chabre, Y.; Vaughan, G.; Amatucci, G. G.; Leriche, J. B.; Patoux, S.; Masquelier, C.; Tarascon, J. M. *Electrochim. Acta* **2002**, *47*, 3137−3149.

(35) Nytén, A.; Kamali, S.; Haggstrom, L.; Gustafsson, T.; Thomas, J. O. *J. Mater. Chem.* **2006**, *16*, 2266.

(36) Yoon, W.-S.; Grey, C. P.; Balasubramanian, M.; Yang, X.-Q.; Fischer, D. A.; McBreen, J. *Electrochem. Solid-State Lett.* **2004**, *7*, A53.

(37) Yamakawa, N.; Jiang, M.; Key, B.; Grey, C. P. *J. Am. Chem. Soc.* **2009**, *131*, 10525−10536.

(38) Hu, Y.-Y.; Liu, Z.; Nam, K. W.; Borkiewicz, O. J.; Cheng, J.; Hua, X.; Dunstan, M. T.; Yu, X.; Wiaderek, K. M.; Du, L.-S.; Chapman, K. W.; Chupas, P. J.; Yang, X.-Q.; Grey, C. P. *Nat. Mater.* **2013**, *12*, 1130−1136.

(39) Wilcke, S. L.; Lee, Y. J.; Cairns, E. J.; Reimer, J. A. *Appl. Magn. Reson.* **2007**, *32*, 547−563.

(40) Hung, I.; Zhou, L.; Pourpoint, F.; Grey, C. P.; Gan, Z. *J. Am. Chem. Soc.* **2012**, *134*, 1898−1901.

(41) Clément, R. J.; Pell, A. J.; Middlemiss, D. S.; Strobridge, F. C.; Miller, J. K.; Whittingham, M. S.; Emsley, L.; Grey, C. P.; Pintacuda, G. *J. Am. Chem. Soc.* **2012**, *134*, 17178−17185.
(42) Strobridge, F. C.; Leskes, M.; Borkiewicz, O.; Wiaderek, K.; Chapman, K.; Chupas, P.; Grey, C. P. Presented at the 224th ECS Meeting, 2013; Abstract #833.
(43) Kaus, M.; Issac, I.; Heinzmann, R.; Doyle, S.; Mangold, S.; Hahn, H.; Chakravadhanula, V. S. K.; Kübel, C.; Ehrenberg, H.; Indris, S. *J. Phys. Chem. C* **2014**, 140709070815007.
(44) Kobayashi, G.; Nishimura, S.-I.; Park, M.-S.; Kanno, R.; Yashima, M.; Ida, T.; Yamada, A. *Adv. Funct. Mater.* **2009**, *19*, 395−403.
(45) Stinton, G. W.; Evans, J. S. O. *J. Appl. Crystallogr.* **2007**, *40*, 87−95.
(46) Borkiewicz, O. J.; Shyam, B.; Wiaderek, K. M.; Kurtz, C.; Chupas, P. J.; Chapman, K. W. *J. Appl. Crystallogr.* **2012**, *45*, 1261−1269.
(47) Lee, P. L.; Shu, D.; Ramanathan, M.; Preissner, C.; Wang, J.; Beno, M. A.; Von Dreele, R. B.; Ribaud, L.; Kurtz, C.; Antao, S. M.; Jiao, X.; Toby, B. H. *J. Synchrotron Radiat.* **2008**, *15*, 427−432.
(48) Kresse, G.; Hafner, J. *Phys. Rev. B* **1993**, *47*, 558−561.
(49) Kresse, G.; Hafner, J. *Phys. Rev. B* **1994**, *49*, 14251−14269.
(50) Kresse, G.; Furthmuller, J. *Comput. Mater. Sci.* **1996**, 15−50.
(51) Kresse, G.; Furthmuller, J. *Phys. Rev. B* **1996**, *54*, 11169−11185.
(52) Hohenberg, P.; Kohn, W. *Phys. Rev.* **1964**, *136*, B864−B871.
(53) Kohn, W.; Sham, J. *Phys. Rev.* **1965**, *140*, A1133−A1138.
(54) Blochl, P. E. *Phys. Rev. B* **1994**, *50*, 17953−17979.
(55) Kresse, G.; Joubert, D. *Phys. Rev. B* **1999**, *59*, 1758−1775.
(56) Perdew, J. P.; Burke, K.; Ernzerhof, M. *Phys. Rev. Lett.* **1996**, *77*, 3865−3868.
(57) Perdew, J. P.; Burke, K.; Ernzerhof, M. *Phys. Rev. Lett.* **1997**, *78*, 3865.
(58) Anisimov, V. I.; Zaanen, J.; Andersen, O. K. *Phys. Rev. B* **1991**, *44*, 943−954.
(59) Anisimov, V. I.; Solovyev, I. V.; Korotin, M.; Czyzyk, M. T.; Sawatzky, G. A. *Phys. Rev. B* **1993**, *48*, 16929−16934.
(60) Liechtenstein, A. I.; Anisimov, V. I.; Zaanen, J. *Phys. Rev. B* **1995**, *52*, R5467−R5470.
(61) Roberts, M. R.; Madsen, A.; Nicklin, C.; Rawle, J.; Palmer, M. G.; Owen, J. R.; Hector, A. L. *J. Phys. Chem. C* **2014**, *118*, 6548−6557.
(62) Snook, G. A.; Huynh, T. D.; Hollenkamp, A. F.; Best, A. S. *J. Electroanal. Chem.* **2012**, *687*, 30−34.
(63) von Cresce, A.; Xu, K. *J. Electrochem. Soc.* **2011**, *158*, A337.
(64) Ravnsbæk, D. B.; Xiang, K.; Xing, W.; Borkiewicz, O. J.; Wiaderek, K. M.; Gionet, P.; Chapman, K. W.; Chupas, P. J.; Chiang, Y. M. *Nano Lett.* **2014**, *14*, 1484−1491.
(65) Middlemiss, D. S.; Ilott, A. J.; Clément, R. J.; Strobridge, F. C.; Grey, C. P. *Chem. Mater.* **2013**, *25*, 1723−1734.
(66) Strobridge, F. C.; Middlemiss, D. S.; Pell, A. J.; Leskes, M.; Clément, R. J.; Pourpoint, F.; Lu, Z.; Hanna, J. V.; Pintacuda, G.; Emsley, L.; Samoson, A.; Grey, C. P. *J. Mater. Chem. A* **2014**.
(67) Grau-Crespo, R.; Hamad, S.; Catlow, C. R. A.; Leeuw, N. H. de. *J. Phys.: Condens. Matter* **2007**, *19*, 256201.
(68) Piao, Y.; Qin, Y.; Ren, Y.; Heald, S. M.; Sun, C.; Zhou, D.; Polzin, B. J.; Trask, S. E.; Amine, K.; Wei, Y.; Chen, G.; Bloom, I.; Chen, Z. *Phys. Chem. Chem. Phys.* **2014**, *16*, 3254.
(69) Cabana, J.; Shirakawa, J.; Chen, G.; Richardson, T. J.; Grey, C. P. *Chem. Mater.* **2010**, *22*, 1249−1262.
(70) Malik, R.; Zhou, F.; Ceder, G. *Nat. Mater.* **2011**, *10*, 587−590.
(71) Van der Ven, A.; Garikipati, K.; Kim, S.; Wagemaker, M. *J. Electrochem. Soc.* **2009**, *156*, A949.
(72) Cogswell, D. A.; Bazant, M. Z. *ACS Nano* **2012**, *6*, 2215−2225.
(73) Delmas, C.; Maccario, M.; Croguennec, L.; Le Cras, F.; Weill, F. *Nat. Mater.* **2008**, *7*, 665−671.
(74) Liu, H.; Strobridge, F. C.; Borkiewicz, O. J.; Wiaderek, K. M.; Chapman, K. W.; Chupas, P. J.; Grey, C. P. *Science* **2014**, *344*, 1252817−1252817.
(75) Zhang, X.; van Hulzen, M.; Singh, D. P.; Brownrigg, A.; Wright, J. P.; van Dijk, N. H.; Wagemaker, M. *Nano Lett.* **2014**, *14*, 2279−2285.
(76) Zhou, F.; Maxisch, T.; Ceder, G. *Phys. Rev. Lett.* **2006**, *97*, 155704.
(77) Zhou, F.; Marianetti, C. A.; Cococcioni, M.; Morgan, D.; Ceder, G. *Phys. Rev. B* **2004**, *69*, 201101.
(78) Arroyo-de Dompablo, M. E.; Amador, U.; Garcia-Alvarado, F. *J. Electrochem. Soc.* **2006**, *153*, A673.
(79) Bacq, O.; Pasturel, A.; Bengone, O. *Phys. Rev. B* **2004**, *69*, 245107.